

Analysis of a shift of the maximum of photoelectron momentum distributions generated by intense circularly polarized pulses

Masataka Ohmi,¹ Oleg I. Tolstikhin,² and Toru Morishita^{1,3}

¹*Department of Engineering Science, The University of Electro-Communications, 1-5-1 Chofu-ga-oka, Chofu-shi, Tokyo 182-8585, Japan*

²*Moscow Institute of Physics and Technology, Dolgoprudny 141700, Russia*

³*Institute for Advanced Science, The University of Electro-Communications, 1-5-1 Chofu-ga-oka, Chofu-shi, Tokyo 182-8585, Japan*

(Received 2 July 2015; published 2 October 2015)

We investigate a shift of the maximum of photoelectron momentum distributions (PEMDs) produced in the ionization of a model atom by intense half-cycle and one-cycle circularly polarized pulses. Our analysis approaches the problem from two complementary directions: by solving the time-dependent Schrödinger equation (TDSE) and by using the adiabatic theory. The TDSE results show that the maximum is shifted along the ridge of the PEMD in the polarization plane from the position corresponding to the maximum of the ionizing field to a later ionization moment. The direction of this longitudinal shift agrees with that observed and discussed in relation to the attoclock technique. In addition, we found a transverse shift of the maximum resulting from the fact that the ridge expands in the radial direction from the position predicted by classical mechanics. The PEMDs obtained from the adiabatic theory are in quantitative agreement with the TDSE results. In particular, the uniform adiabatic asymptotics closely reproduces the transverse shift of the ridge and partially reproduces the longitudinal shift of the maximum of the PEMD. The adiabatic theory also yields a simple analytic formula describing the transverse shift.

DOI: [10.1103/PhysRevA.92.043402](https://doi.org/10.1103/PhysRevA.92.043402)

PACS number(s): 32.80.Fb, 32.80.Rm, 42.50.Hz

I. INTRODUCTION

Circularly polarized laser pulses complement linearly polarized pulses as a tool to generate strong-field phenomena, providing an alternative perspective to study the underlying dynamics. One of the main differences stems from the fact that electrons ionized and driven by a circularly polarized field do not return to the parent ion, and hence there is no rescattering [1]. This enables one to observe processes that otherwise would be masked or contaminated by a signal caused by rescattering. For example, circular polarization is essential for accurate measurements of the orientation dependence of tunneling ionization rates of molecules [2,3]. Circularly polarized pulses also suggest new experimental schemes for molecular imaging [4] and new theoretical techniques [5] to extract molecular structure information from the observable photoelectron momentum distribution (PEMD). The PEMD in this case has a donutlike shape [6]. One of the most striking achievements with circularly polarized pulses in recent years is the demonstration of an attoclock [7]. The possibility of improving the time resolution down to a fraction of the laser period (2.7 fs for $\lambda = 800$ nm) results from the nonuniformity of PEMDs generated by ultrashort few-cycle pulses in the toroidal direction. Classical mechanics maps the angular coordinate in this direction to the ionization moment. In a related experiment [8] a shift of the maximum of the PEMD from the position corresponding to the maximum of the ionizing field was observed. Since this feature is important for the attoclock operation, it has attracted much theoretical attention [9–12].

In this paper we calculate and analyze PEMDs produced in the ionization of an atom by intense half-cycle and one-cycle circularly polarized pulses. The goal and virtue of the work is threefold. First, we introduce and demonstrate an efficient scheme to solve the time-dependent Schrödinger equation (TDSE) capable of treating arbitrary polarization of the laser

field. Our approach is based on a combination of the Lanczos propagator [13,14] in time, partial-wave expansion in angular variables, and a finite-element discrete variable representation (FEDVR) [15–17] in radial coordinate. We believe that this approach may have advantages over other methods [9,18–20] in extending calculations for pulses with general elliptic polarization to stronger fields and lower frequencies. Second, we compare the TDSE results with the predictions of the adiabatic theory [21]. The asymptotic formulas for the PEMD obtained in Ref. [21] apply to any polarization. So far, they were implemented and validated by calculations only for linearly polarized pulses. The present work illustrates the performance of the adiabatic theory in the circular polarization case. Third, armed by the numerical results and analytical approximations based on the adiabatic theory we investigate the topography of the PEMD in the polarization plane. We focus on the positions of a nearly circular ridge of the PEMD and its global maximum along the ridge. The very short duration of the pulses considered (in terms of the number of optical cycles) is explained by the wish to make these features distinct and avoid their distortion by interference structures. We find that in addition to a longitudinal shift of the maximum along the ridge similar to the one observed in Ref. [8], there is also a transverse shift caused by the fact that the ridge expands in the radial direction with respect to its position predicted by classical mechanics. There exist controversial opinions [9–12] regarding the effect of the Coulomb tail of the atomic potential on the longitudinal shift. For definiteness, in this work we exclude this effect by considering a model atom described by a finite-range potential. The adiabatic theory analysis of the shifts of the maximum of the PEMD yields the main physical results of this work.

The paper is organized as follows. Section II introduces our model. In Sec. III we outline our numerical method to solve the TDSE. Only the general scheme of the method

is discussed in the main text, more technical details are deferred to the appendixes. Appendix A defines the Radau and Lobatto quadratures. Appendix B describes the construction of the FEDVR radial basis. Appendix C details the present implementation of the R -matrix method to construct scattering states conjugate with the procedure to solve the TDSE. In Sec. IV the problem is treated in the framework of the adiabatic theory [21]. Here we summarize basic equations of the theory needed to calculate the PEMD in the present model (Sec. IV A), discuss some aspects of their numerical implementation (Sec. IV B), and develop analytical approximations describing the main features of the PEMD in focus here (Sec. IV C). In Sec. V, we present and discuss illustrative numerical results. Section VI concludes the paper.

II. MODEL

We consider an electron interacting with a spherically symmetric atomic potential $V(r)$ and an electric field $\mathbf{F}(t)$ of an intense low-frequency laser pulse. The TDSE in the dipole approximation and length gauge reads (atomic units are used throughout)

$$i \frac{\partial \psi(\mathbf{r}, t)}{\partial t} = H(t) \psi(\mathbf{r}, t), \quad (1)$$

where

$$H(t) = -\frac{1}{2} \Delta + V(r) + \mathbf{F}(t) \cdot \mathbf{r}. \quad (2)$$

To exclude the effect of the Coulomb tail of the potential on the features of the PEMD discussed below, in this paper we consider a screened Coulomb potential,

$$V(r) = -\frac{\exp[-(r/10)^2]}{r}. \quad (3)$$

The same model was used to illustrate the adiabatic theory in Ref. [21]. This potential supports three s and two p bound states; the lowest d state appears as a narrow resonance. The electron is assumed to be initially in the ground $1s$ state whose energy $E_0 = -0.485483$ is slightly higher than that in the purely Coulomb potential. The corresponding eigenfunction is denoted by $\phi_0(r)$, so the initial condition for Eq. (1) is

$$\psi(\mathbf{r}, t \rightarrow -\infty) = \phi_0(r) e^{-iE_0 t}. \quad (4)$$

The field is presented in the form $\mathbf{F}(t) = F(t) \mathbf{e}(t)$, where $F(t) \geq 0$ is the field strength and $\mathbf{e}(t)$ is the polarization vector satisfying $\mathbf{e}^2(t) = 1$. We consider pulses propagating along the y axis with circular polarization in the (x, z) plane,

$$\mathbf{e}(t) = \mathbf{e}_x \sin \omega t + \mathbf{e}_z \cos \omega t. \quad (5)$$

The function $F(t)$ is modeled by

$$F(t) = F_0 \exp[-(2t/T)^2]. \quad (6)$$

Thus a pulse is characterized by its amplitude F_0 , angular frequency ω , and duration T . The PEMD is defined by

$$P(\mathbf{k}) = |I(\mathbf{k})|^2, \quad I(\mathbf{k}) = \langle \psi_{\mathbf{k}}^{(-)} | \psi(t \rightarrow \infty) \rangle, \quad (7)$$

where $I(\mathbf{k})$ is the ionization amplitude and $\psi_{\mathbf{k}}^{(-)}(\mathbf{r})$ is the scattering *out* eigenstate of the field-free Hamiltonian with the asymptotic momentum \mathbf{k} normalized by $\langle \psi_{\mathbf{k}}^{(-)} | \psi_{\mathbf{k}}^{(-)} \rangle = (2\pi)^3 \delta(\mathbf{k} - \mathbf{k}')$ [22,23].

III. NUMERICAL SOLUTION OF THE TIME-DEPENDENT SCHRÖDINGER EQUATION

We have developed an efficient numerical scheme to solve Eq. (1) for arbitrary polarization of the laser field. Our approach is based on a combination of the Lanczos method for propagation in time, partial-wave expansion in angular variables, and a FEDVR for treating the radial coordinate. The main advantage of this approach is that it ensures fast convergence and thus enables one to control the accuracy of the results. Here we briefly outline the scheme; more technical details are given in Appendixes A–C.

The time propagator is constructed by the Lanczos method [13,14]. The propagation of the state vector from t to $t + \delta t$ through a small time step δt is approximated by

$$|\psi(t + \delta t)\rangle \approx \exp[-iH(t)\delta t] |\psi(t)\rangle. \quad (8)$$

The error of this approximation scales as δt^2 , but for propagation through the whole time interval it becomes of order δt^3 , provided that $\mathbf{F}(t \rightarrow \pm\infty) = \mathbf{0}$. To evaluate the right-hand side of Eq. (8), we introduce a Krylov subspace spanned by the states

$$|Q_i(t)\rangle = H^{i-1}(t) |\psi(t)\rangle, \quad i = 1, \dots, K, \quad (9)$$

and an orthonormal basis in this subspace $|q_i(t)\rangle$ generated by the Gram-Schmidt process,

$$|Q'_i(t)\rangle = |Q_i(t)\rangle - \sum_{j=1}^{i-1} |q_j(t)\rangle \langle q_j(t) | Q_i(t)\rangle, \quad (10a)$$

$$|q_i(t)\rangle = \frac{|Q'_i(t)\rangle}{\sqrt{\langle Q'_i(t) | Q'_i(t)\rangle}}. \quad (10b)$$

The right-hand side of Eq. (8) is approximated by its projection onto the Krylov subspace and expanded in terms of the basis,

$$\exp[-iH(t)\delta t] |\psi(t)\rangle \approx \sum_{i=1}^K A_i(t, \delta t) |q_i(t)\rangle. \quad (11)$$

The error of this approximation scales as δt^K . To find the expansion coefficients, we diagonalize the Hamiltonian in the Krylov subspace by solving the eigenvalue problem

$$\sum_{j=1}^K [\langle q_i(t) | H(t) | q_j(t)\rangle - \lambda_k(t) \delta_{ij}] Z_{jk}(t) = 0. \quad (12)$$

The coefficients in Eq. (11) are given in terms of the eigenvalues $\lambda_k(t)$ and the eigenvectors $Z_{jk}(t)$ by

$$A_i(t, \delta t) = \sum_{k=1}^K Z_{ik}(t) e^{-i\lambda_k(t)\delta t} Z_{k1}(t). \quad (13)$$

We have analyzed the convergence of this procedure with respect to the time step δt and the dimension of the Krylov subspace K . Our strategy is to maximize δt under the condition that the error incurred by Eq. (8) remains negligible, and then to achieve convergence in Eq. (11) by increasing K . One could expect that this can be done with $K \sim 2$, since in this case the error terms in Eqs. (8) and (11) have the same order in δt , but our calculations show that the convergence of Eq. (11) requires $K \gg 1$. In this situation there is no sense in trying to reduce

the error term in Eq. (8) by increasing its order in δt , which justifies our use of the simplest form of the time propagator in this equation. The Hamiltonian matrix in Eq. (12) is real and tridiagonal [13,14], so even for large K this equation can be easily solved by using standard linear algebra packages. The most time consuming part in implementing Eq. (11) is the construction of the states (9).

To facilitate the calculations in Eq. (9), we adopt a matrix-vector representation for the operators and states involved provided by the partial-wave expansion and the radial FEDVR based on the Radau and Lobatto quadratures [15–17] (see Appendixes A and B). Equation (1) is solved in a spherical box of radius r_m . The time-dependent wave function $\psi(\mathbf{r}, t) = \langle \mathbf{r} | \psi(t) \rangle$ is sought in the form

$$\psi(\mathbf{r}, t) = \sum_{n=1}^N \sum_{l=0}^L \sum_{m=-l}^l C_{nlm}(t) \Pi_n(r) Y_{lm}(\hat{\mathbf{r}}), \quad (14)$$

where $\Pi_n(r)$, $n = 1, \dots, N$, are the FEDVR basis functions orthonormal in the interval $r \in [0, r_m]$, $Y_{lm}(\hat{\mathbf{r}})$ are the spherical harmonics, and L is the maximum angular momentum included in the calculations. Substituting Eq. (14) into Eq. (9), we arrive at simple algebraic equations defining the states $|Q_i(t)\rangle$ in terms of the coefficients $C_{nlm}(t)$. For example, for $i = 2$ we obtain

$$\langle \Pi_n Y_{lm} | Q_2(t) \rangle = \sum_{n'l'm'} H_{nlm, n'l'm'}(t) C_{n'l'm'}(t), \quad (15)$$

where the Hamiltonian matrix is

$$H_{nlm, n'l'm'}(t) = \langle \Pi_n Y_{lm} | H(t) | \Pi_{n'} Y_{l'm'} \rangle. \quad (16)$$

The explicit form of this matrix is given in Appendix B. The FEDVR provides a high rate of convergence with respect to the dimension N of the radial basis. An additional advantage of this representation is that the Hamiltonian matrix is nearly block diagonal and very sparse with only a few percent of nonzero elements, so the matrix-vector multiplications in Eq. (9) can be efficiently implemented.

The initial state $\phi_0(r)$ in Eq. (4) is obtained by diagonalizing the field-free Hamiltonian in the same FEDVR basis. The scattering states $\psi_{\mathbf{k}}^{(-)}(\mathbf{r})$ are given by [22,23]

$$\psi_{\mathbf{k}}^{(-)}(\mathbf{r}) = 4\pi \sum_{l=0}^L \sum_{m=-l}^l i^l e^{-i\delta_l} f_{kl}(r) Y_{lm}^*(\hat{\mathbf{k}}) Y_{lm}(\hat{\mathbf{r}}). \quad (17)$$

Here $f_{kl}(r)$ is the regular solution of the radial equation

$$\left[-\frac{1}{2r^2} \frac{d}{dr} r^2 \frac{d}{dr} + \frac{l(l+1)}{2r^2} + V(r) - \frac{k^2}{2} \right] f_{kl}(r) = 0 \quad (18)$$

satisfying the asymptotic boundary condition

$$f_{kl}(r \geq r_m) = j_l(kr) \cos \delta_l - y_l(kr) \sin \delta_l, \quad (19)$$

where $j_l(x)$ and $y_l(x)$ are the spherical Bessel functions [24] and δ_l is the partial-wave phase shift. We solve Eq. (18) using the R -matrix method; for further details see Appendix C. The scattering states are thus obtained at the same FEDVR radial quadrature points r_n as used in solving Eq. (1), so the integration in Eq. (7) can be easily carried out. The working

formula for calculating the PEMD is

$$P(\mathbf{k}) = \left| 4\pi \sum_{n=1}^N \sum_{l=0}^L \sum_{m=-l}^l i^{-l} e^{i\delta_l} \times \sqrt{\Omega_n} C_{nlm}(t \rightarrow \infty) f_{kl}(r_n) Y_{lm}(\hat{\mathbf{k}}) \right|^2, \quad (20)$$

where Ω_n are the FEDVR quadrature weights and the values of $f_{kl}(r_n)$ are given in Eq. (C12).

This numerical scheme is characterized by relatively few parameters, namely, the time step δt , the dimension of the Krylov subspace K , the radius of the spherical box r_m , and the numbers of partial waves L and the FEDVR basis functions N in the expansion (14). For each laser pulse considered below, we have varied all the parameters to achieve convergence of the PEMD. Their typical values used in the calculations are $\delta t = 0.01$, $K = 1000$, $r_m = 300$, $N = 700$, and $L = 120$. We mention that this scheme can be readily generalized to potentials with a Coulomb tail as well as to molecular potentials without spherical symmetry, provided that the partial-wave expansion converges.

IV. ADIABATIC THEORY

Let T_0 be the characteristic time of the laser field in Eq. (1). For pulses defined by Eqs. (5) and (6) we have $T_0 = \min(T, 2\pi/\omega)$. Let ΔE be the energy spacing between the initial state and the nearest eigenstate of the unperturbed atom. In the present model ΔE is close to the ionization potential $|E_0| = \alpha^2/2$. Then the adiabatic parameter $\epsilon = 2\pi/\Delta E T_0$ gives the ratio of the atomic and laser field time scales. Small values of this parameter correspond to the adiabatic regime. The adiabatic theory amounts to the asymptotic solution of Eq. (1) for $\epsilon \rightarrow 0$. This theory was developed for finite-range potentials and arbitrary polarization of the laser field in Ref. [21]. The second key parameter of the theory $\xi = F_0 \alpha / \Delta E$ characterizes the strength of the laser field. The adiabatic approximation holds under the condition

$$\epsilon \ll \min(\xi^2, 1). \quad (21)$$

Thus the asymptotics is uniform in ξ , that is, the theory applies to weak (underbarrier, $\xi \ll 1$) as well as strong (overbarrier, $\xi \gtrsim 1$) fields, provided that ϵ is sufficiently small.

The adiabatic theory as the asymptotics defined above can be compared with other theories in the field that rely on the adiabatic approximation. These are the Keldysh theory [25] and its developments in Refs. [26,27], modifications of the Keldysh theory proposed by Faisal [28] and Reiss [29] and known as the strong-field approximation (SFA), and some further extensions of the SFA in Refs. [30,31]. Let us mention three main differences; for more details see Refs. [21,32]. First, in contrast to the Keldysh theory and SFA, the adiabatic theory takes into account the interaction with the laser field in the initial state. This interaction leads to the Stark shift and depletion of the initial state—the effects that become important for sufficiently long and/or intense pulses. Second, the adiabatic theory fully takes into account the interaction with the atomic potential in the final state. This leads to the appearance of the exact scattering amplitude in the

asymptotics of the PEMD, while in the SFA the scattering characteristics can appear only in the Born approximation [30]. Third, the adiabatic theory can treat arbitrarily strong fields under the condition (21), while the Keldysh theory and SFA in the tunneling regime in spite of the name of the latter approximation apply only to weak fields satisfying $\epsilon \ll \xi \ll 1$ [21]. Thus the adiabatic theory is quite different from the Keldysh theory and its extensions.

The adiabatic theory yields the asymptotic solution of Eq. (1) from which all the observables can be deduced. In particular, the PEMD was obtained in Ref. [21]. In this section we summarize formulas needed to calculate the PEMD in the present model (Sec. IV A), discuss their implementation (Sec. IV B), and analyze the topography of the PEMD in the polarization plane (Sec. IV C). The latter analysis yields results that are in the focus of the present study.

A. Photoelectron momentum distribution

In the adiabatic theory [21] the ionization amplitude in Eq. (7) is obtained in the form $I(\mathbf{k}) = I_a(\mathbf{k}) + I_r(\mathbf{k})$, where the two terms represent the adiabatic and rescattering parts, respectively. The derivation of the adiabatic part is based on the assumption that after ionization the electron does not interact with the atomic potential $V(r)$ and its further motion is driven only by the field. The rescattering part accounts for this interaction. Its contribution is appreciable (and even becomes dominant in certain regions of the photoelectron momentum space) only if the ionized electron returns back and hits the region of localization of $V(r)$. However, this does not happen for circularly polarized pulses, so in the present study we neglect $I_r(\mathbf{k})$ and consider only $I_a(\mathbf{k})$. This amplitude is given by [21]

$$I_a(\mathbf{k}) = e^{i\pi/4} (2\pi)^{1/2} \sum_i \frac{A_0(\Delta\mathbf{k}_\perp^+; t_i^+)}{F^{1/2}(t_i^+)} \times \exp \left[i\mathcal{S}(t_i^+, \mathbf{k}) - is_0(t_i^+) - \frac{i\Delta k_\parallel^3}{3F(t_i^+)} \right]. \quad (22)$$

The notation here are defined in terms of quantities of two kinds, quantum and classical. The quantum quantities are the properties of the Siegert state (SS) in a static electric field $\mathbf{F} = F\mathbf{e}$ [33–35] originating from the initial bound state of the unperturbed atom. For spherically symmetric potentials they are functions of the field strength F only and do not depend on its direction \mathbf{e} . Equation (22) involves the complex SS energy eigenvalue $E_0(F)$ and the transverse momentum distribution (TMD) amplitude $A_0(\mathbf{k}_\perp; F)$, where \mathbf{k}_\perp is orthogonal to \mathbf{e} . These functions can be calculated for any complex F using the program developed in Ref. [33]; their behavior for the present potential (3) is discussed and illustrated in Ref. [21]. They should be taken at the instantaneous value of the field $F(t)$, and thus become functions of time denoted by $E_0(t) = E_0(F(t))$ and $A_0(\mathbf{k}_\perp; t) = A_0(\mathbf{k}_\perp; F(t))$. From Eq. (6) we have $E_0(t \rightarrow \pm\infty) = E_0$. The quantum action in Eq. (22) is

$$s_0(t) = E_0 t + \int_{-\infty}^t [E_0(t') - E_0] dt'. \quad (23)$$

The second term here accounts for both the accumulation of an additional phase by the initial state due to the Stark shift

and its depletion via tunneling or over-the-barrier ionization. The classical quantities are expressed in terms of the velocity for a reference classical electron trajectory in the field $\mathbf{F}(t)$,

$$\mathbf{v}(t) = - \int_{-\infty}^t \mathbf{F}(t') dt', \quad \mathbf{v}(t \rightarrow \infty) = \mathbf{v}_\infty. \quad (24)$$

The classical action in Eq. (22) is

$$\mathcal{S}(t, \mathbf{k}) = \frac{1}{2} \mathbf{k}^2 t - \frac{1}{2} \int_t^\infty [\mathbf{u}_i^2(t', \mathbf{k}) - \mathbf{k}^2] dt', \quad (25)$$

where

$$\mathbf{u}_i(t, \mathbf{k}) = \mathbf{k} - \mathbf{k}_a(t) \quad (26)$$

and

$$\mathbf{k}_a(t) = \mathbf{v}_\infty - \mathbf{v}(t). \quad (27)$$

The vector $\mathbf{u}_i(t, \mathbf{k})$ gives the initial velocity with which an electron driven by the field should start its motion at moment t to have the final velocity at $t \rightarrow \infty$ equal to \mathbf{k} . This velocity turns to zero at $\mathbf{k} = \mathbf{k}_a(t)$, therefore a curve \mathcal{K}_a in the photoelectron momentum space traced by the end of $\mathbf{k}_a(t)$ as t varies along the real axis represents the classical support of the PEMD. Since $d\mathbf{k}_a(t) = \mathbf{F}(t)dt$, the field $\mathbf{F}(t)$ is tangential to the curve \mathcal{K}_a at the point $\mathbf{k} = \mathbf{k}_a(t)$. The quantum and classical quantities meet in the saddle-point equation defining the moments of ionization for a given \mathbf{k} ,

$$\frac{1}{2} \mathbf{u}_i^2(t, \mathbf{k}) - E_0(t) = 0 \quad \rightarrow \quad t = t_i^\pm(\mathbf{k}), \quad (28)$$

where the subscript i enumerates the solutions. The solutions appear in pairs lying in the upper (+) and lower (−) halves of the complex time plane [see Eq. (33) below]. The summation over i in Eq. (22) includes all physically meaningful solutions in the upper half plane; for brevity, we have omitted the argument of $t_i^\pm(\mathbf{k})$. In the adiabatic regime the length of \mathcal{K}_a is $O(\epsilon^{-1})$ and the PEMD $P(\mathbf{k})$ is localized in a narrow pipeline neighborhood K_a of \mathcal{K}_a of width $O(\epsilon^0)$. Then each $\mathbf{k} \in K_a$ can be presented in the form

$$\mathbf{k} = \mathbf{k}_a(t_i^+) + \Delta\mathbf{k}^+, \quad \Delta\mathbf{k}^+ = \Delta k_\parallel^+ \mathbf{e}(t_i^+) + \Delta\mathbf{k}_\perp^+, \quad (29)$$

where the parallel and perpendicular components of $\Delta\mathbf{k}^+$ refer to the direction of $\mathbf{e}(t_i^+)$. From Eqs. (26) and (29) we have $\mathbf{u}_i(t_i^+, \mathbf{k}) = \Delta\mathbf{k}^+$, thus Δk_\parallel^+ and $\Delta\mathbf{k}_\perp^+$ give the longitudinal and transverse components of the initial velocity of an electron at the moment of ionization t_i^+ with respect to the instantaneous direction of the electric field. Note that $\Delta\mathbf{k}^+$ is generally complex, since t_i^+ is complex. This defines the remaining notation in Eq. (22).

Equation (22) gives the asymptotics of $I_a(\mathbf{k})$ for $\epsilon \rightarrow 0$ that is uniform in ξ . If the limit $\epsilon \rightarrow 0$ is considered for a fixed ξ , then this asymptotics can be simplified and takes the form [21]

$$I_a(\mathbf{k}) = e^{i\pi/4} (2\pi)^{1/2} \sum_i \frac{A_0(\Delta\mathbf{k}_\perp; t_i)}{F^{1/2}(t_i)} \exp [i\mathcal{S}(t_i, \mathbf{k}) - is_0(t_i)]. \quad (30)$$

Here the moments of ionization are defined by

$$\mathbf{e}(t)\mathbf{u}_i(t, \mathbf{k}) = 0 \quad \rightarrow \quad t = t_i(\mathbf{k}), \quad (31)$$

and the summation runs over all physically meaningful solutions to this equation. Similarly to Eq. (29), each $\mathbf{k} \in K_a$

can be presented in the form

$$\mathbf{k} = \mathbf{k}_a(t_i) + \Delta\mathbf{k}_\perp. \quad (32)$$

Now the initial velocity at the moment of ionization $\mathbf{u}_i(t_i, \mathbf{k}) = \Delta\mathbf{k}_\perp$ is real and orthogonal to $\mathbf{e}(t_i)$. In the adiabatic regime the different solutions of Eq. (31) lie at a distance $O(\epsilon^{-1})$ from each other. In this case there exists a correspondence between the solutions of Eqs. (28) and (31) for the same i : t_i^\pm can be found at a distance $O(\epsilon^0)$ from t_i and are given by [21]

$$t_i^\pm = t_i \pm i \frac{[\Delta\mathbf{k}_\perp^2 - 2E_0(t_i)]^{1/2}}{F(t_i)} + O(\epsilon^1). \quad (33)$$

Equation (30) is the leading-order term in the expansion of Eq. (22) in the difference $t_i^+ - t_i$ (which amounts to the expansion in ϵ ; see Sec. IV C). As seen from Eq. (33), this difference becomes large for sufficiently weak fields. In this case the approximation employed in the step from Eq. (22) to Eq. (30) does not hold, but Eq. (22) remains applicable, provided that the condition (21) is satisfied. In the following, we call Eqs. (22) and (30) the *uniform* and *simple* asymptotics of $I_a(\mathbf{k})$, respectively.

B. Saddle points

To implement Eqs. (22) and (30) one needs to solve the saddle-point equations (28) and (31), respectively. It should be understood that these equations generally have infinitely many solutions in the complex t plane, but only few of them are physically meaningful and should be included in the sums in Eqs. (22) and (30). This issue deserves a discussion.

To find the physical saddle points for a given photoelectron momentum \mathbf{k} , one should consider only the real solutions of Eq. (31). Such solutions can be easily found by plotting the left-hand side of Eq. (31) as a function of t . For each solution $t_i(\mathbf{k})$, one should try to find the corresponding solution $t_i^+(\mathbf{k})$ of Eq. (28). We do this by the Newton-Raphson method with $t_i(\mathbf{k})$ used as the initial guess. Equation (33) approximately predicts the location of $t_i^+(\mathbf{k})$. To proceed by the Newton-Raphson iterations from $t_i(\mathbf{k})$ to $t_i^+(\mathbf{k})$ the left-hand side of Eq. (28) should be analytically continued along the path. The continuation of the first term does not cause any problems since the field $\mathbf{F}(t)$ is known analytically and the velocity $\mathbf{v}(t)$ defined by Eq. (24) is a single-valued function that can be easily calculated for any complex t . The continuation of $E_0(t)$ is less straightforward. As explained above, the SS energy eigenvalue $E_0(F)$ becomes a function of time $E_0(t)$ by substituting $F = F(t)$. The function $E_0(F)$ is a branch of a multivalued function $E(F)$ whose different branches correspond to the different SSs. To select the branch corresponding to the given initial state one has to cut the complex F plane along some lines emanating from each branch point connecting the initial state with other SSs. We found many such branch points for the present model located in the fourth quadrant of the F plane; similar branch points for the Coulomb potential were found in Ref. [36]. The images of the branch cuts in the t plane can be met in the analytic continuation of $E_0(t)$ from $t_i(\mathbf{k})$ to $t_i^+(\mathbf{k})$. If this happens, the Newton-Raphson iterations should be terminated. Because if they are continued through the cut and eventually converge to a solution of Eq. (28), this solution

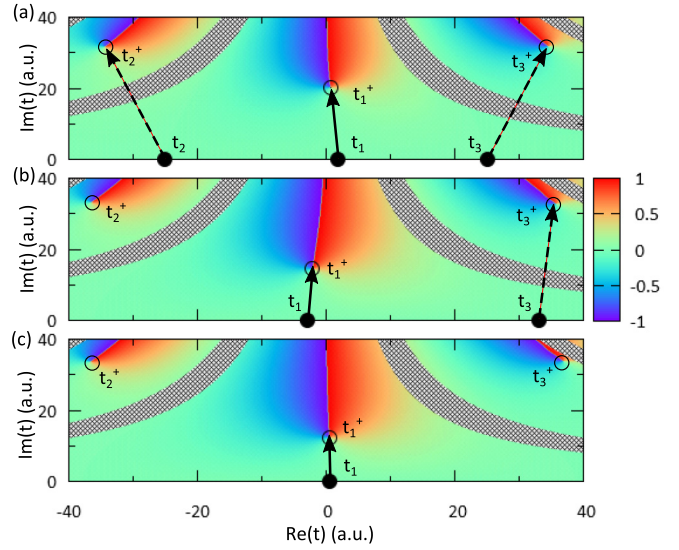


FIG. 1. (Color online) The argument (in units of π) of the left-hand side of Eq. (28) as a function of complex time for a half-cycle pulse with $F_0 = 0.07$, $\omega = 0.063$, and $T = 50$, hence $v_0 = 1.13$, calculated at (a) $\mathbf{k}/v_0 = (-0.18, -0.71)$, (b) $\mathbf{k}/v_0 = (-0.58, -0.89)$, and (c) $\mathbf{k}/v_0 = (-0.89, -0.71)$. The saddle points $t_i(\mathbf{k})$ and $t_i^+(\mathbf{k})$ defined by Eqs. (31) and (28) are shown by solid and open circles, respectively. Arrows connect the corresponding saddle points according to Eq. (33). Hatched stripes indicate branch cut regions of the Siegert-state energy $E_0(t)$, where $-\pi/2 \leq \arg F(t) \leq -\pi/3$. In all three cases, only $t_1(\mathbf{k})$ and $t_1^+(\mathbf{k})$ are physical saddle points.

should be deemed *unphysical*, since it belongs to a different branch of $E(F)$.

Let us illustrate this discussion by calculations for one of the pulses treated in Sec. V. Figure 1 shows the argument of the left-hand side of Eq. (28) as a function of complex time for three representative values of the photoelectron momentum \mathbf{k} . The solutions of Eq. (28) can be clearly seen in the plot as origins of the lines where the argument jumps by 2π . For this pulse $T = 50$, so the field strength (6) as a function of real t is well localized in the interval $-40 \leq t \leq 40$ considered in Fig. 1. The number of the solutions of Eq. (31) in this interval depends on \mathbf{k} . Figure 2 shows regions in the \mathbf{k} space where Eq. (31) has one, two, and three solutions in the specified interval.

Before we proceed, let us comment on the notation. For the present polarization (5) the vectors (24) and (27), and hence the classical support \mathcal{K}_a of the PEMD, lie in the (k_x, k_z) plane which is parallel to the polarization plane. In the calculations reported below we set $k_y = 0$ and consider PEMDs only in this plane. Then it is convenient to omit the y component of all the vectors and simply write $\mathbf{k} = (k_x, k_z)$, etc. In addition, to bring PEMDs for the different pulses to a common scale in the \mathbf{k} space, it is convenient to measure momenta in units of the characteristic velocity $v_0 = F_0/\omega$. We thus have $\mathbf{v}_\infty = (0, v_\infty)$, where

$$v_\infty = -\frac{\sqrt{\pi}}{2} \omega T \exp\left[-\frac{\omega^2 T^2}{16}\right] v_0. \quad (34)$$

The curve \mathcal{K}_a is shown by the white line in Fig. 2; it begins at $\mathbf{k} = \mathbf{v}_\infty$ ($t \rightarrow -\infty$, left end) and ends at $\mathbf{k} = (0, 0)$ ($t \rightarrow +\infty$,

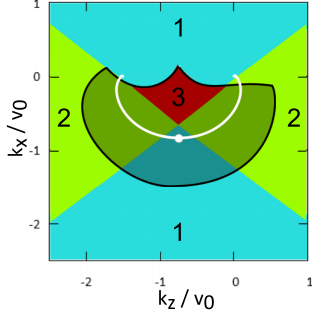


FIG. 2. (Color online) For the same pulse as in Fig. 1, Eq. (31) has one, two, and three real solutions $t_i(\mathbf{k})$ in the interval $-40 \leq t \leq 40$ in the blue, green, and red regions of the (k_x, k_z) plain, respectively. The white line shows the classical support \mathcal{K}_a of the PEMD given by the trace of $\mathbf{k}_a(t)$ as t varies along the real axis. The solid white circle indicates the point $\mathbf{k}_a(0)$ corresponding to the maximum of the ionizing field. The shaded area indicates the region where the condition $|\Delta \mathbf{k}_\perp^+ / \Delta k_\parallel^+| \leq 0.8$ is satisfied [see Eqs. (29)]; only inside this region the uniform adiabatic results are calculated. The PEMD for this pulse is shown in Fig. 4.

right end). This explains the format of Fig. 2 and the PEMD plots to follow.

Returning to Fig. 1, the values of $E_0(F)$ at complex F used to make this plot were calculated in two steps. First, we calculate $E_0(F)$ along the ray $\arg F = 0$, by starting from the energy E_0 of the unperturbed initial state at $F = 0$ and making small steps in $|F|$, thus ensuring the continuity of the function $E_0(F)$. Second, we continue $E_0(F)$ from the ray $\arg F = 0$ by small steps in $\arg F$ to a given complex point F . Only the sector $|\arg F| \leq \pi/2$ is considered; further continuation is accomplished by substituting $F \rightarrow -F$, which implies simultaneous change of the sign of \mathbf{e} . Using this procedure, the branch points discussed above are found in the sector $-\pi/2 \leq \arg F \leq -\pi/3$. The image of this sector in the complex t plane calculated using Eq. (6) is shown by hatched stripes in Fig. 1; these stripes are called the *branch cut regions*. The upper panel in Fig. 1 illustrates the case when Eq. (31) has three solutions in the interval $-40 \leq t \leq 40$. For t_1 there exists the corresponding solution of Eq. (28) belonging to the same branch $E_0(F)$ of the SS energy eigenvalue. For t_2 and t_3 there also exist the corresponding solutions of Eq. (28) near the locations predicted by Eq. (33), but these solutions belong to different SSs since they are separated from t_2 and t_3 by branch cut regions. In this case there is only one pair of physical saddle points, t_1 and t_1^+ . The middle panel in Fig. 1 shows the case when Eq. (31) has two solutions in the specified interval. The pair t_1 and t_1^+ is physical, while the pair t_3 and t_3^+ is unphysical and should not be included in the sums in Eqs. (30) and (22). Note that in this case there exists another unphysical solution t_2^+ of Eq. (28) that has no counterpart among the real solutions of Eq. (31). The bottom panel in Fig. 1 shows the case when Eq. (31) has one solution. Again, the saddle points t_1 and t_1^+ are physical, while t_2^+ and t_3^+ are unphysical. In this way we conclude that for the present pulse Eqs. (28) and (31) have only one pair of physical solutions indicated by t_1 and t_1^+ in the figure for all values of \mathbf{k} . Let the region adjacent to the real time axis and bounded from above by the branch cut regions

be called the *physical time sheet*. Then the above discussion can be simply summarized as follows: only the solutions of Eqs. (28) and (31) that appear together with their counterpart defined by Eq. (33) on the physical time sheet represent the physically meaningful saddle points that should be included in the sums in Eqs. (22) and (30).

There is an additional technical issue arising in the calculations of the saddle points that should be mentioned. As \mathbf{k} moves away from \mathcal{K}_a , the decomposition of $\Delta \mathbf{k}^+$ in Eqs. (29) into its parallel and perpendicular components with respect to $\mathbf{e}(t_i^+)$ loses its meaning. In other words, Eq. (22) applies only in the vicinity of \mathcal{K}_a . This is consistent with the fact that in the adiabatic regime the PEMD $P(\mathbf{k})$ is localized near the curve \mathcal{K}_a . In our calculations, we use the empirical criterion $|\Delta \mathbf{k}_\perp^+ / \Delta k_\parallel^+| \leq 0.8$ to define the region in the \mathbf{k} space where Eq. (22) applies. For the pulse discussed above, this region is shown by the shaded area in Fig. 2; only in this region the uniform asymptotics (22) is implemented. The simple asymptotics (30) can be calculated for any $\Delta \mathbf{k}_\perp$ in Eq. (32).

C. Topography of the photoelectron momentum distribution

Here we investigate the structure of the distribution $P(\mathbf{k})$ characterized by the region of its localization and topography. In particular, we analyze the positions of the ridge of the PEMD in the (k_x, k_z) plane and its global maximum along the ridge. In the adiabatic regime these features are essentially determined by the TMD amplitude $A_0(\mathbf{k}_\perp; F)$, the other factors in Eqs. (22) and (30) are less important. The behavior of this function can be understood from its weak-field asymptotics [37] which for the present model is given by

$$A_0(\mathbf{k}_\perp; F) = e^{i\pi/4} \frac{2\pi C}{\chi^{1/2}} \exp\left(-\frac{\chi^3}{3F} - \frac{\chi \mathbf{k}_\perp^2}{2F}\right), \quad (35)$$

where $C = re^{x^r} \phi_0(r)|_{r \rightarrow \infty} \approx 3.832$. The ionization rate $\Gamma_0(F) = -2 \text{Im}[E_0(F)]$ in the same approximation is [37,38]

$$\Gamma_0(F) = \int |A_0(\mathbf{k}_\perp; F)|^2 \frac{d\mathbf{k}_\perp}{(2\pi)^2} = \frac{\pi C^2 F}{\chi^2} \exp\left(-\frac{2\chi^3}{3F}\right). \quad (36)$$

When Eq. (35) is substituted into Eqs. (22) and (30), its exponent should be combined with the exponents in these equations. We are not interested in the oscillatory structure of $P(\mathbf{k})$ that may result from an interference of the contributions from the different saddle points, only in the shape of its envelope. Then it is sufficient to consider only the real part of the resulting exponent.

We begin with the simple asymptotics (30). In this case the real part is

$$-\frac{\chi^3}{3F(t_i)} - \frac{1}{2} \int_{-\infty}^{t_i} \Gamma_0(t) dt - \frac{\chi \Delta \mathbf{k}_\perp^2}{2F(t_i)}, \quad (37)$$

where $\Gamma_0(t) = \Gamma_0(F(t))$. It is convenient to consider the moment of ionization t_i and the initial electron velocity $\Delta \mathbf{k}_\perp$ as ‘‘curvilinear coordinates’’ in the region of localization \mathcal{K}_a of the PEMD longitudinal and transverse with respect to its classical support \mathcal{K}_a . The last term in Eq. (37) shows that $P(\mathbf{k})$ as a function of $\Delta \mathbf{k}_\perp$ attains a maximum at $\Delta \mathbf{k}_\perp = \mathbf{0}$, that is, when \mathbf{k} belongs to \mathcal{K}_a . Thus $P(\mathbf{k})$ has a ridge along

\mathcal{K}_a (see the white line in Fig. 2). The width of this ridge in $\Delta \mathbf{k}_\perp$ is determined by that of the TMD amplitude and in the weak-field case is $\sim \sqrt{F(t_i)/\chi}$. The first and second terms in Eq. (37) represent the instantaneous ionization rate and survival probability, respectively. Their balance determines the position of the global maximum of $P(\mathbf{k})$ along the ridge. Let us temporarily neglect depletion. Then the maximum is attained when $t_i = 0$, which corresponds to the maximum of the field (6), and is located at $\mathbf{k} = \mathbf{k}_a(0)$. This point is shown by the white circle in Fig. 2. Taking into account depletion shifts the maximum to an *earlier* ionization moment $t_i < 0$ defined by $\dot{F}(t_i)/F^2(t_i) = 3\Gamma_0(t_i)/2\chi^3$ (here and in the following, dots denote differentiation with respect to time), that is, to the left of the white circle in Fig. 2 along the line \mathcal{K}_a . If the shift of the maximum in \mathbf{k} space is small, it can be found analytically and for the present pulse is given by

$$-\frac{3F_0^2 T^2 \Gamma(F_0)}{16\chi^3} \mathbf{e}_z. \quad (38)$$

To see whether this shift is significant, the coefficient of \mathbf{e}_z should be compared with v_0 . This coefficient grows with T and may become $\sim v_0$ for sufficiently strong fields and long pulses. However, since $\Gamma(F_0)$ rapidly varies with F_0 and is exponentially small for weak fields, the actual value of the shift is very sensitive to the field amplitude. A shift of the maximum of the PEMD from the maximum of the ionizing field caused by depletion was seen in calculations for circularly polarized pulses [18]. A similar shift exists in the linear polarization case [21].

We now turn to the uniform asymptotics (22). As mentioned above, Eq. (30) gives the leading-order term in the expansion of Eq. (22) for $\epsilon \rightarrow 0$. To analyze the difference between the two asymptotics and its effect on the topography of the PEMD, we extend the expansion to the first-order terms. To this end, we need to extend the expansion (33),

$$t_i^+ - t_i = \delta_0 + \delta_1 + O(\epsilon^2), \quad (39a)$$

$$\delta_0 = \frac{i}{F(t_i)} [\Delta \mathbf{k}_\perp^2 - 2E_0(t_i)]^{1/2} = O(\epsilon^0), \quad (39b)$$

$$\delta_1 = \frac{1}{F(t_i)} \left[\frac{\dot{E}_0(t_i)}{F(t_i)} - \frac{1}{2} \delta_0^2 \dot{F}(t_i) + \frac{1}{2} \delta_0 \dot{\delta}_0(t_i) \Delta \mathbf{k}_\perp \right] = O(\epsilon^1). \quad (39c)$$

The leading-order term δ_0 here agrees with Eq. (33). Let the exponents in Eqs. (22) and (30) (not including the TMD amplitude) be denoted by iS_i^+ and iS_i , respectively. We have

$$S_i^+ - S_i = \int_{t_i}^{t_i^+} \left[\frac{1}{2} \mathbf{u}_i^2(t, \mathbf{k}) - E_0(t) \right] dt - \frac{\Delta k_\parallel^+{}^3}{3F(t_i^+)}. \quad (40)$$

Using Eqs. (39) we obtain

$$S_i^+ - S_i = \Delta_1 + O(\epsilon^2), \quad (41a)$$

$$\begin{aligned} \Delta_1 &= F(t_i) \delta_0^2 \left[\frac{\dot{E}_0(t_i)}{2F(t_i)} - \frac{5}{24} \delta_0^2 \dot{F}(t_i) - \frac{2}{3} \delta_0 \dot{\delta}_0(t_i) \Delta \mathbf{k}_\perp \right] \\ &= O(\epsilon^1). \end{aligned} \quad (41b)$$

Note that the terms $O(\epsilon^0)$ in Eq. (41a) cancel, as expected. To see the effect of this difference on the position of the ridge

of $P(\mathbf{k})$, it should be expanded near \mathcal{K}_a up to linear terms in $\Delta \mathbf{k}_\perp$. In addition, since the analytic expression for the TMD amplitude (35) is available only in the weak-field case, the weak-field approximation should be used also in Eq. (41b). We thus obtain

$$\Delta_1 = \frac{\chi^3}{F^2(t_i)} \left[-\frac{5\chi \dot{F}(t_i)}{24F(t_i)} + \frac{2i}{3} \dot{\mathbf{e}}(t_i) \Delta \mathbf{k}_\perp \right]. \quad (42)$$

Similar expansion for the exponent from Eq. (35) in Eq. (22) is

$$\begin{aligned} &-\frac{\chi^3}{3F(t_i^+)} - \frac{\chi \Delta \mathbf{k}_\perp^2}{2F(t_i^+)} \\ &= \left[-\frac{\chi^3}{3F(t_i)} - \frac{\chi \Delta \mathbf{k}_\perp^2}{2F(t_i)} \right] \\ &+ \frac{i\chi^4 \dot{F}(t_i)}{3F^3(t_i)} + \frac{\chi^3}{2F^2(t_i)} \dot{\mathbf{e}}(t_i) \Delta \mathbf{k}_\perp + O(\epsilon^2). \end{aligned} \quad (43)$$

The bracket here is the exponent of the TMD amplitude in Eq. (30), and the following terms represent the first-order difference we seek. Combining together all these expansions, for the real part of the resulting exponent in Eq. (22) we again obtain Eq. (37) where, however, the $\Delta \mathbf{k}_\perp$ in the last term is replaced by

$$\Delta \mathbf{k}_\perp + \frac{\chi^2 \dot{\mathbf{e}}(t_i)}{6F(t_i)}. \quad (44)$$

Note that the second term on the right-hand side cannot be obtained simply by expanding $\Delta \mathbf{k}_\perp^+$ from Eq. (29), since it absorbed also the last term from Eq. (42). The ridge of $P(\mathbf{k})$ is now located where the vector (44) turns to zero. Let us introduce

$$\mathbf{k}_a^+(t) = \mathbf{k}_a(t) - \frac{\chi^2 \dot{\mathbf{e}}(t)}{6F(t)}, \quad (45)$$

and let \mathcal{K}_a^+ denote a curve in the \mathbf{k} space traced by the end of $\mathbf{k}_a^+(t)$. This curve gives the new position of the ridge. For circularly polarized pulses $\dot{\mathbf{e}}(t_i)$ is orthogonal to $\mathbf{e}(t_i)$, points inwards the curve \mathcal{K}_a , and its length is equal to ω [see Eq. (5)]. Thus \mathcal{K}_a^+ is expanded from \mathcal{K}_a in the radial direction outwards by $\chi^2 \omega / 6F(t)$. The first two terms in Eq. (37) remain unchanged in the first order in ϵ , so there is no an additional shift of the global maximum of $P(\mathbf{k})$ along the ridge.

Summarizing, the simple asymptotics (30) predicts that the PEMD has a ridge along the curve \mathcal{K}_a and its global maximum is shifted along the ridge from the momentum $\mathbf{k}_a(0)$ corresponding to the maximum of the field to earlier ionization times. This longitudinal shift is caused by depletion and approximately given by Eq. (38). The uniform asymptotics (22) predicts that the ridge of the PEMD is shifted from \mathcal{K}_a in the transverse direction outwards and is located along the curve \mathcal{K}_a^+ . In the first order in ϵ , the transverse shift is described by the second term in Eq. (45). No additional longitudinal shift appears in this order.

V. RESULTS AND DISCUSSION

In this section we present numerical results for PEMDs obtained from Eq. (7) by solving the TDSE (1) and by

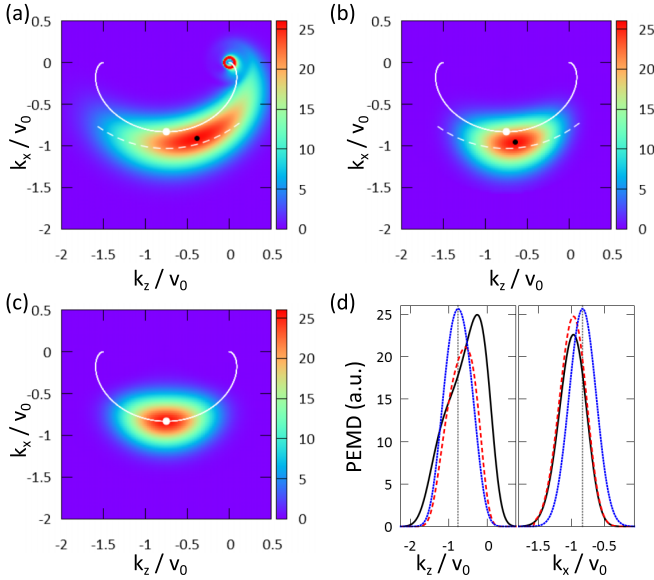


FIG. 3. (Color online) PEMD $P(k_x, k_y = 0, k_z)$ for a half-cycle pulse with $F_0 = 0.07$, $\omega = 0.079$, and $T = 40$. For this pulse $v_0 = 0.90$. Panel (a) and solid (black) lines in (d): TDSE results. Panel (b) and dashed (red) lines in (d): uniform adiabatic approximation, Eq. (22). Panel (c) and dotted (blue) lines in (d): simple adiabatic approximation, Eq. (30). The uniform and simple adiabatic results are multiplied by 1.39 and 1.78, respectively. Solid white lines in (a), (b), and (c) show the classical support \mathcal{K}_a of the PEMD given by the trace of $\mathbf{k}_a(t)$, Eq. (27). Solid white circles indicate the position of $\mathbf{k}_a(0)$ corresponding to the maximum of $F(t)$. Dashed white lines in (a) and (b) show the shifted ridge \mathcal{K}_a^+ given by the trace of $\mathbf{k}_a^+(t)$, Eq. (45). Solid black circles indicate the actual position of the global maximum of the distribution. Panel (d) shows cuts of the PEMDs through the point $\mathbf{k}_a(0)$; the vertical dotted lines in the left and right subpanels indicate the position of $k_{az}(0)$ and $k_{ax}(0)$, respectively. The survival probability is 0.990.

implementing the uniform (22) and simple (30) asymptotic formulas of the adiabatic theory [21]. The PEMDs are calculated for $k_y = 0$ and considered in the (k_x, k_z) plain. To avoid a distortion of the topography of the distribution $P(\mathbf{k})$ by interference effects, we consider ultrashort half-cycle and one-cycle pulses defined by Eqs. (5) and (6) with frequencies and durations related by $\omega T = \pi$ and 2π , respectively. In all the cases, the saddle-point equations (28) and (31) have only one physical solution, so the sums in Eqs. (22) and (30) contain only one term. The peak pulse intensity is given in terms of the field amplitude by $I = cF_0^2/4\pi$. We consider pulses with two amplitudes, $F_0 = 0.1/\sqrt{2} \approx 0.07$ ($I = 3.51 \times 10^{14}$ W/cm²) and $F_0 = 0.1$ ($I = 7.02 \times 10^{14}$ W/cm²), both below the critical field $F_c \approx 0.12$ giving a boundary between tunneling and over-the-barrier ionization for the present model [21].

We first consider half-cycle pulses with $\omega T = \pi$. In this case $v_\infty/v_0 \approx -1.502$ and $\mathbf{k}_a(0)/v_0 = (-0.832, -0.751)$. Two parameter sets are treated: $T = 40$, hence $\omega = \pi/40 \approx 0.079$ ($\lambda \approx 580$ nm), and $T = 50$, hence $\omega = \pi/50 \approx 0.063$ ($\lambda \approx 725$ nm). The calculations are done for four pulses obtained by combining these two frequencies with the two field amplitudes indicated above. The results are presented in Figs. 3–6. We are interested in both the absolute magnitude

and the shape of the distribution $P(\mathbf{k})$. The magnitude is characterized by the value of $P(\mathbf{k})$ at its maximum. To facilitate the comparison of the shapes of the different results for the same pulse, the adiabatic results are multiplied by constant factors to make their values at the maximum equal to that of the TDSE results; these factors are given in captions to the figures.

All the main features to be observed are seen already in Fig. 3. The TDSE results are shown in Fig. 3(a). The maximum (solid black circle) of the PEMD is shifted from $\mathbf{k}_a(0)$ (solid white circle). This shift can be decomposed into the longitudinal and transverse components with respect to \mathcal{K}_a (solid white curve). In the longitudinal direction, the maximum is shifted to the right, that is, to a *later* ionization moment with respect to the maximum of the field. The direction of this shift is opposite to that of the depletion shift (38) and agrees with the direction of a shift observed in Ref. [8]. We mention that the depletion shift is very small for all four pulses under consideration; the TDSE results for the probability to survive in the initial state are given in captions to the figures. The very existence of the longitudinal shift for the present finite-range potential is in contradiction with the conclusions of Ref. [12]. In addition to the longitudinal shift there exists a transverse shift. The ridge of the PEMD in Fig. 3(a) is clearly shifted from \mathcal{K}_a outwards; its position is fairly well reproduced by \mathcal{K}_a^+ (dashed white curve). The open red circle seen in the upper right corner of Fig. 3(a) is a true physical feature representing a narrow $3d$ resonance supported by the potential (3); this feature is beyond our current interest and we do not discuss it here; for more details see Ref. [21]. The uniform and simple adiabatic results are shown in Figs. 3(b) and 3(c), respectively. The present pulse corresponds to the largest ω and the smallest F_0 among the four half-cycle pulses considered, which is least favorable for the adiabatic approximation [see Eq. (21)]. The uniform and simple asymptotics underestimate the value of $P(\mathbf{k})$ at its maximum by 28% and 44%, respectively. Thus the uniform asymptotics works better. It also gives a better prediction for the shape of the distribution $P(\mathbf{k})$. In particular, the ridge of the PEMD in Fig. 3(b) is shifted from \mathcal{K}_a outwards and well described by \mathcal{K}_a^+ . The maximum of the PEMD has also a longitudinal shift in the right direction, but its magnitude is noticeably smaller than the longitudinal shift in Fig. 3(a). The ridge of the simple adiabatic results in Fig. 3(c) coincides with \mathcal{K}_a and the maximum of the PEMD almost coincides with $\mathbf{k}_a(0)$, since depletion is negligible. Let us emphasize that Eq. (45) defining \mathcal{K}_a^+ gives only an approximation for the true position of the ridge of the uniform adiabatic results valid up to terms of the first order in ϵ . The accurate numerical implementation of the uniform asymptotics (22) is in much better agreement with the TDSE results than Eq. (45). This is seen in Fig. 3(d), which shows the horizontal (left subpanel) and vertical (right subpanel) cuts of the three PEMDs through the point $\mathbf{k}_a(0)$. The longitudinal shifts of the maxima of the TDSE (solid black lines) and uniform adiabatic (dashed red lines) results can be clearly seen in the left subpanel. The right subpanel shows a perfect agreement between the corresponding transverse shifts. The cuts of the simple adiabatic PEMD (dotted blue lines) peak at $\mathbf{k}_a(0)$.

Figure 4 shows similar results for a pulse with the same amplitude as in Fig. 3 but 20% lower frequency. All the

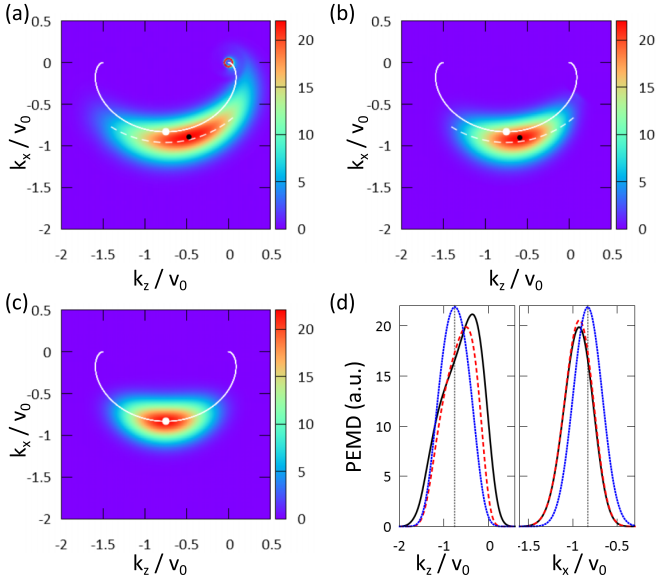


FIG. 4. (Color online) Same as in Fig. 3, but for a half-cycle pulse with $F_0 = 0.07$, $\omega = 0.063$, and $T = 50$, hence $v_0 = 1.13$. The uniform and simple adiabatic results are multiplied by 1.18 and 1.53, respectively. The survival probability is 0.987.

features discussed above remain qualitatively unchanged, but the quantitative agreement between the TDSE and adiabatic results becomes better. The uniform and simple asymptotics underestimate the value of $P(\mathbf{k})$ at its maximum by 15% and 35%, respectively. The longitudinal shift of the uniform adiabatic results is now closer to that of the TDSE results. The transverse shift seen in the right subpanel of Fig. 4(d) is again perfectly reproduced. The ridges of the TDSE and uniform adiabatic PEMDs are located closer to the curve \mathcal{K}_a^+ . Figure 5 shows results for a pulse with the same frequency as

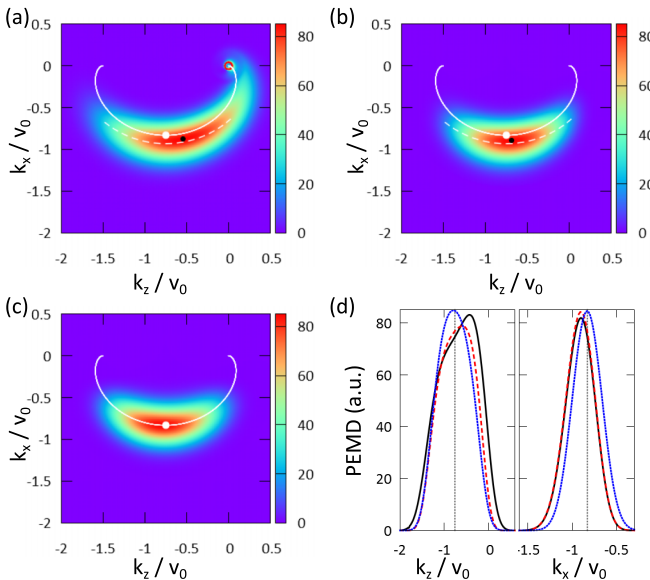


FIG. 5. (Color online) Same as in Fig. 3, but for a half-cycle pulse with $F_0 = 0.1$, $\omega = 0.079$, and $T = 40$, hence $v_0 = 1.27$. The uniform and simple adiabatic results are multiplied by 1.24 and 1.00, respectively. The survival probability is 0.867.

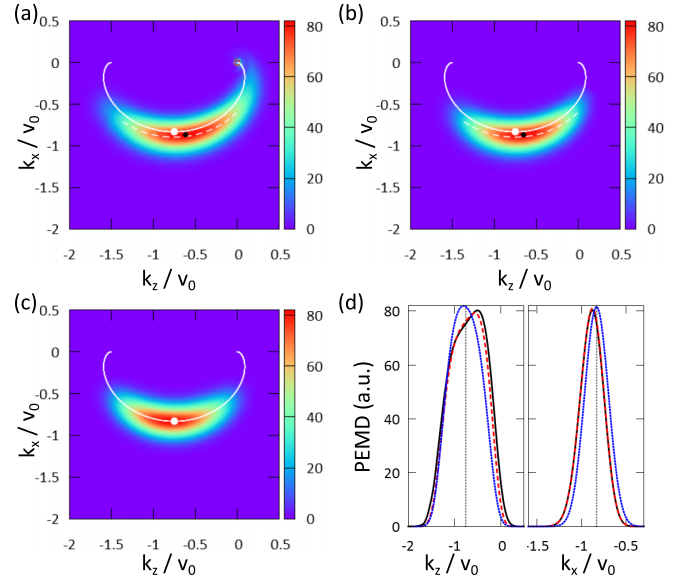


FIG. 6. (Color online) Same as in Fig. 3, but for a half-cycle pulse with $F_0 = 0.1$, $\omega = 0.063$, and $T = 50$, hence $v_0 = 1.59$. The uniform and simple adiabatic results are multiplied by 1.12 and 0.98, respectively. The survival probability is 0.836.

in Fig. 3 but 41% larger amplitude. The uniform asymptotics underestimates the value of $P(\mathbf{k})$ at its maximum by 19%, which is slightly larger than the error in Fig. 4, while the simple asymptotics perfectly reproduces the correct value. Such a difference in the behavior of the uniform and simple adiabatic results is explained by the fact that although both approximations converge to the TDSE results as $\omega \rightarrow 0$, the rate of their convergence depends on F_0 and is different for the two asymptotics. The longitudinal shift in Fig. 5(b) is smaller than that in Fig. 5(a). Figure 6 shows results for the last half-cycle pulse considered. The field amplitude in this pulse is larger and the frequency is smaller compared to Fig. 3, both changes being favorable for the adiabatic approximation. The uniform asymptotics underestimates the value of $P(\mathbf{k})$ at its maximum by 11%, while the simple asymptotics overestimates it by 2%. The uniform asymptotics closely reproduces the shape of the PEMD as well as the positions of its ridge and maximum, as is seen from the cuts in Fig. 6(d). A small longitudinal depletion shift (to the left in the figure) of the maximum of the simple adiabatic results can be noticed in the left subpanel.

In the half cycle pulses discussed above, we have varied the amplitude and frequency of the pulse, keeping its shape unchanged. To explore the modification of the reference PEMD shown in Fig. 3 in one more direction, we consider a one-cycle pulse with the same amplitude and frequency as in Fig. 3, but with $T = 80$, hence $\omega T = 2\pi$. For this pulse $v_\infty/v_0 \approx -0.472$ and $\mathbf{k}_a(0)/v_0 = (-1.282, -0.236)$. The results are shown in Fig. 7. The uniform and simple asymptotics underestimate the value of $P(\mathbf{k})$ at its maximum by 10% and 39%, respectively. Both the longitudinal and transverse shifts are present in the TDSE and uniform adiabatic results. The agreement between these results is almost as good as in Fig. 6, better than for the half-cycle pulse in Fig. 3. We recall that Fig. 7(a) is obtained by solving the TDSE,

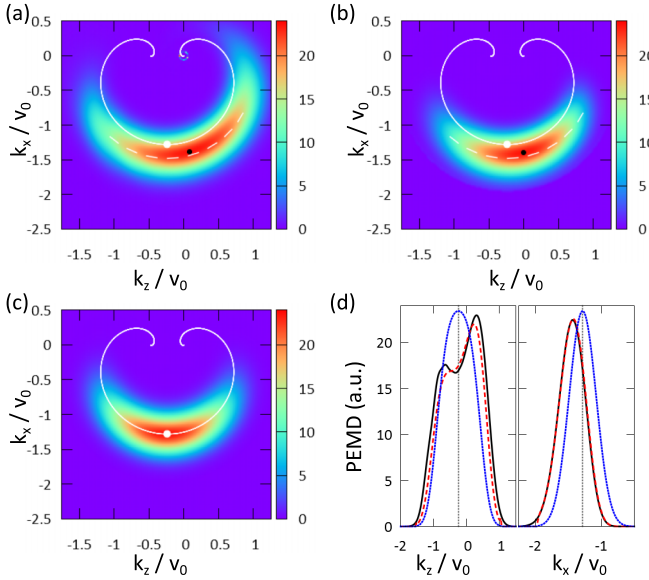


FIG. 7. (Color online) Same as in Fig. 3, but for a one-cycle pulse with $F_0 = 0.07$, $\omega = 0.079$, and $T = 80$, hence $v_0 = 0.90$. The uniform and simple adiabatic results are multiplied by 1.11 and 1.64, respectively. The survival probability is 0.979.

Eq. (1), while Fig. 7(b) is calculated by implementing an analytical formula, Eq. (22). This level of agreement between the TDSE and adiabatic results within 10% is consistent with Ref. [21]. It illustrates the performance of the adiabatic theory for circularly polarized pulses. We mention that the SFA is known to reproduce, at best, only the shape of the PEMD, but not its magnitude. For example, the TDSE and SFA results for circularly polarized pulses reported in Ref. [9] differ by orders of magnitude. Moreover, the SFA does not reproduce any longitudinal or transverse shift.

To conclude the discussion of Figs. 3–7, we note that the shifts of the maximum of the PEMD from $\mathbf{k}_a(0)$ in both directions with respect to \mathcal{K}_a seen in the TDSE results decrease as F_0 grows and/or ω decreases. Such a behavior of the transverse shift is in agreement with Eq. (45). This observation is also consistent with the general prediction of the adiabatic theory that only the depletion shift survives in the limit $\epsilon \rightarrow 0$.

The extension of the present TDSE calculations to lower frequencies is possible, but becomes rather time consuming. On the other hand, the implementation of the uniform asymptotics (22) becomes easier as ω decreases, because the saddle points defined by Eq. (28) become better separated and it is easier to find them. Taking into account the good performance of Eq. (22) already for the pulses considered, this equation can be used instead of the TDSE in calculations for lower frequencies. In the deep adiabatic limit, when $\omega \rightarrow 0$ for a fixed value of ωT , the uniform asymptotics converges to the simple asymptotics (30) whose implementation is even easier. It is instructive to illustrate the convergence of the two asymptotics. This is done in Figs. 8 and 9. Here we consider half-cycle pulses with $\omega = \pi/100 \approx 0.031$ ($\lambda \approx 1450$ nm) and $\omega = \pi/200 \approx 0.015$ ($\lambda \approx 2900$ nm), in both cases $\omega T = \pi$. The agreement between the uniform and simple adiabatic results rapidly improves as ω decreases and for the pulse in Fig. 9 it becomes virtually perfect. Note that, except for the uniform results shown in Fig. 8(a), there appears a depletion shift (to the left in the figures) of the maximum of the PEMD, while the transverse shift becomes negligible, as seen in the right subpanels in Figs. 8(c) and 9(c). Thus Eq. (30) provides an ultimate theoretical tool for extending strong-field physics from the near-infrared through mid-infrared [39] to the terahertz [40] range.

VI. CONCLUSIONS

We have introduced and demonstrated an efficient method to solve the TDSE for arbitrary polarization of the laser field. The method has a high rate of convergence and ensures high accuracy of the results. We believe this method may be advantageous in extending the current calculations for pulses with general elliptic polarization [9,18–20] to higher intensities and lower frequencies. We have also implemented the adiabatic theory [21] for circularly polarized pulses and compared its predictions with the TDSE results. The uniform and simple adiabatic asymptotics are shown to converge to the TDSE results and to each other on the quantitative level as the pulse frequency decreases. This validates both our numerical method and the adiabatic theory for the circular polarization case; for linearly polarized pulses, the theory

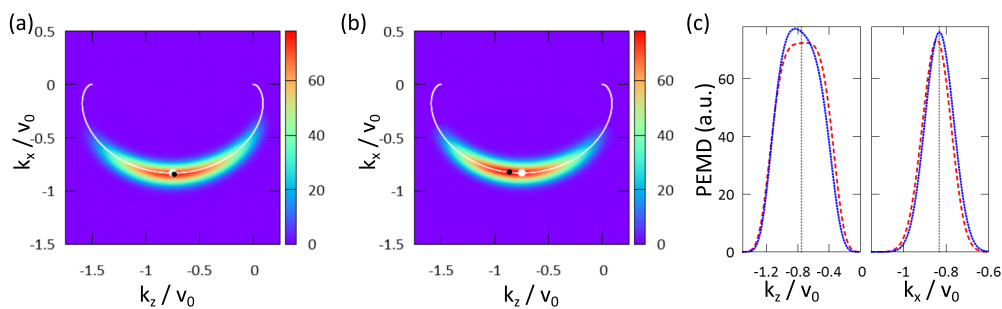


FIG. 8. (Color online) PEMD $P(k_x, k_y = 0, k_z)$ for a half-cycle pulse with $F_0 = 0.1$, $\omega = 0.031$, and $T = 100$, hence $v_0 = 3.18$. Panel (a) and dashed (red) lines in (c): uniform adiabatic approximation, Eq. (22). Panel (b) and dotted (blue) lines in (c): simple adiabatic approximation, Eq. (30). The results are not multiplied by any factor. Solid white lines in (a) and (b) show the classical support \mathcal{K}_a of the PEMD given by the trace of $\mathbf{k}_a(t)$, Eq. (27). Solid white circles indicate the position of $\mathbf{k}_a(0)$ corresponding to the maximum of $F(t)$. Solid black circles indicate the actual position of the global maximum of the distribution. Panel (c) shows cuts of the PEMDs through the point $\mathbf{k}_a(0)$; the vertical dotted lines in the left and right subpanels indicate the position of $k_{az}(0)$ and $k_{ax}(0)$, respectively. The survival probability is 0.699.

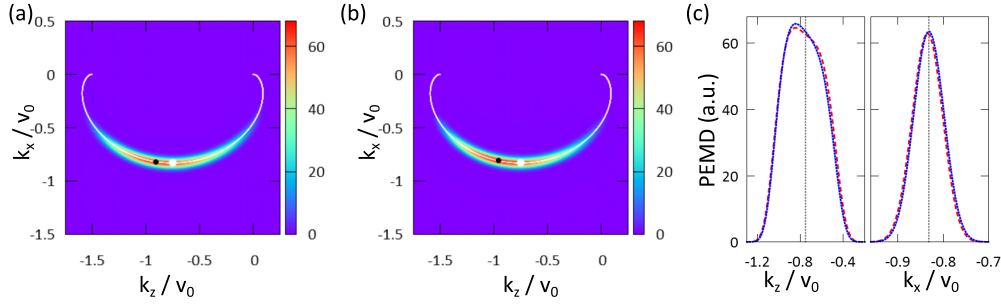


FIG. 9. (Color online) Same as in Fig. 8, but for a half-cycle pulse with $F_0 = 0.1$, $\omega = 0.015$, and $T = 200$, hence $v_0 = 6.37$. The survival probability is 0.488.

has been tested by calculations in Ref. [21]. On the basis of these technical developments we investigated a shift of the maximum of PEMDs generated by half-cycle and one-cycle pulses. The shift in the TDSE results can be decomposed into the longitudinal and transverse components with respect to the ridge of the PEMD in the polarization plane. The longitudinal component shifts the maximum from the position corresponding to the maximum of the ionizing field to later ionization times. This agrees with the direction of the longitudinal shift observed in Ref. [8]. In addition, we found a transverse shift that results from the fact that the ridge of the PEMD expands in the radial direction outwards from its position determined by classical mechanics. The uniform adiabatic approximation closely reproduces the transverse shift. It also predicts some longitudinal shift in the right direction whose magnitude, however, is in less convincing agreement with the TDSE results. The simple adiabatic approximation accounts only for the depletion part of the longitudinal shift whose direction is opposite to that observed in Ref. [8] and does not predict any transverse shift. Only the depletion shift survives in the deep adiabatic regime, all the other contributions to the shift are caused by nonadiabatic effects. By expanding the uniform asymptotics near the simple asymptotics up to terms of the first order in the adiabatic parameter ϵ , we obtained an analytic formula (45) describing the transverse shift which is shown to be in good agreement with the numerical results. But no new longitudinal shift in addition to that caused by depletion appears in this order. The latter conclusion, although negative, is a rigorous statement within the adiabatic theory.

The transverse shift of the ridge of the PEMD found in the present numerical calculations and described by the adiabatic theory is a feature that one should take into account in the analysis of experimental results. Since the shift is inversely proportional to the field amplitude, see Eq. (45), by measuring it one can find the field intensity. The shift also depends on the ionization potential, so tunneling ionization from inner orbitals produces donutlike contributions to the PEMD of larger radii. In principle, this may enable one to separate electrons ionized from the different orbitals, which is not possible with linearly polarized pulses, although averaging over the focal volume may hinder such a separation.

ACKNOWLEDGMENTS

We thank L. B. Madsen for useful discussions on the subjects of Refs. [9–11]. This work was supported in part

by JSPS KAKENHI Grants No. 26400415 and No. 10500598. O.I.T. acknowledges support from the Russian Foundation for Basic Research (Grant No. 14-02-92110) and the Ministry of Education and Science of Russia (State Assignment No. 3.679.2014/K).

APPENDIX A: RADAU AND LOBATTO QUADRATURES

Similarly to the Gauss-Legendre quadrature, the Gauss-Radau and Gauss-Lobatto quadratures [41] approximate the integral of a smooth function $f(x)$ over the interval $x \in [-1, 1]$,

$$\int_{-1}^1 f(x) dx \approx \sum_{i=1}^N \omega_i f(x_i), \quad (\text{A1})$$

where x_i and ω_i are the quadrature points and weights, respectively. In the Legendre case, the x_i and ω_i are defined by the requirement that Eq. (A1) becomes exact when $f(x)$ is a polynomial of degree $2N - 1$ or less. This approach can be generalized to the case when $n \leq N$ quadrature points have fixed positions in the interval. The remaining $N - n$ quadrature points and all the weights can then be defined by requiring that Eq. (A1) is exact for polynomials of degree not higher than $2N - 1 - n$. The Radau quadrature corresponds to $n = 1$ with the fixed quadrature point at the right end of the interval, $x_N = 1$. The other quadrature points are the zeros of $[P_N(x) - P_{N-1}(x)]/(1 - x)$, where $P_n(x)$ are the Legendre polynomials [24]. The corresponding weights are given by

$$\omega_i = \frac{1 + x_i}{N^2 P_{N-1}^2(x_i)}. \quad (\text{A2})$$

The Lobatto quadrature corresponds to $n = 2$ with fixed quadrature points at both ends of the interval, $x_1 = -1$ and $x_N = 1$. The other quadrature points are the zeros of $dP_{N-1}(x)/dx$ and the corresponding weights are

$$\omega_i = \frac{2}{N(N-1)P_{N-1}^2(x_i)}. \quad (\text{A3})$$

For an arbitrary interval of integration $x \in [a, b]$, these quadrature points and weights are modified as

$$x_i \rightarrow \frac{b+a}{2} + \frac{b-a}{2} x_i, \quad \omega_i \rightarrow \frac{b-a}{2} \omega_i. \quad (\text{A4})$$

APPENDIX B: FINITE-ELEMENT DISCRETE VARIABLE REPRESENTATION

The FEDVR approach amounts to the finite-element (FEM) method [42] combined with a discrete variable representation (DVR) [43–45] used inside the elements. Equation (1) is considered in a finite spherical box of radius r_m . To construct the FEDVR radial basis, the interval $r \in [0, r_m]$ is divided into N_s sectors, $0 = \bar{r}_0 \leq \dots \leq \bar{r}_s \leq \dots \leq \bar{r}_{N_s} = r_m$. Inside each sector $r \in [\bar{r}_{s-1}, \bar{r}_s]$, $s = 1, \dots, N_s$, the N_p -point DVR basis is introduced,

$$\pi_i^s(r) = \frac{1}{\sqrt{\omega_i^s}} \prod_{\substack{j=1 \\ j \neq i}}^{N_p} \frac{r - r_j^s}{r_i^s - r_j^s}, \quad (\text{B1})$$

where r_i^s and ω_i^s , $i = 1, \dots, N_p$, are the corresponding quadrature points and weights. The DVR basis functions have the property

$$\pi_i^s(r_j^s) = \delta_{ij} / \sqrt{\omega_i^s}. \quad (\text{B2})$$

To connect the neighboring sectors within the FEM method they must have a quadrature point at their common boundary. To satisfy this requirement, we use the Radau quadrature with a quadrature point at the right end of the sector, in the first sector ($s = 1$), and the Lobatto quadrature with quadrature points at both ends of the sector, in subsequent sectors ($s > 1$). These quadratures are defined in Appendix A. The collection of all quadrature points r_n is enumerated by

$$n = (s - 1)(N_p - 1) + i; \quad (\text{B3})$$

their total number is $N = N_s(N_p - 1) + 1$. The associated weights Ω_n and the global FEDVR basis functions $\Pi_n(r)$ are

defined as follows. For $n = (s - 1)(N_p - 1) + N_p$ with $s = 1, \dots, N_s - 1$, which corresponds to quadrature points at the boundaries between sectors, we set $\Omega_n = \omega_{N_p}^s + \omega_1^{s+1}$ and

$$\Pi_n(r) = \frac{1}{\sqrt{\Omega_n}} \begin{cases} \sqrt{\omega_{N_p}^s} \pi_{N_p}^s(r), & r \in [\bar{r}_{s-1}, \bar{r}_s], \\ \sqrt{\omega_1^{s+1}} \pi_1^{s+1}(r), & r \in [\bar{r}_s, \bar{r}_{s+1}]. \end{cases} \quad (\text{B4})$$

This function bridges the sectors s and $s + 1$ and is continuous through the boundary between them (but its derivative is not). For the other values of n , corresponding to quadrature points inside sectors and the one at the outer boundary $r_N = r_m$ of the box, we set $\Omega_n = \omega_i^s$ and

$$\Pi_n(r) = \pi_i^s(r), \quad r \in [\bar{r}_{s-1}, \bar{r}_s]. \quad (\text{B5})$$

Thus constructed FEDVR basis satisfies

$$\Pi_n(r_{n'}) = \delta_{nn'} / \sqrt{\Omega_n}. \quad (\text{B6})$$

Using this property and the quadrature r_n , Ω_n , $n = 1, \dots, N$, for any smooth function $f(r)$ we obtain

$$\int_0^{r_m} \Pi_n(r) f(r) \Pi_{n'}(r) dr \approx f(r_n) \delta_{nn'}. \quad (\text{B7})$$

In particular, this shows that the FEDVR basis is orthonormal in the interval $r \in [0, r_m]$. Thus the main properties of a DVR [43–45] given by Eqs. (B6) and (B7) are preserved.

The functions $\Pi_n(r) Y_{lm}(\hat{\mathbf{r}})$ provide an orthonormal basis in the spherical box $r \leq r_m$. The matrix elements of the Hamiltonian (2) in this basis defined by Eq. (16) are given by

$$H_{nlm, n'l'm'}(t) = \left[K_{nn'} + \left(\frac{l(l+1)}{2r_n^2} + V(r_n) \right) \delta_{nn'} \right] \delta_{ll'} \delta_{mm'} + F(t) r_n \delta_{nn'} (\mathcal{S}_{lm, l'm'} \sin \omega t + \mathcal{C}_{lm, l'm'} \cos \omega t). \quad (\text{B8})$$

The radial kinetic energy matrix is

$$K_{nn'} = \frac{1}{2r_n r_{n'}} \sum_{k=1}^N \Omega_k \left. \frac{d\Pi_n(r)}{dr} r^2 \frac{d\Pi_{n'}(r)}{dr} \right|_{r=r_k}, \quad (\text{B9})$$

where the derivatives of the FEDVR basis functions can be found using

$$\left. \frac{d\pi_i^s(r)}{dr} \right|_{r=r_j^s} = \frac{1}{\sqrt{\omega_i^s}} \begin{cases} \frac{1}{r_i^s - r_j^s} \prod_{\substack{k=1 \\ k \neq i, j}}^{N_p} \frac{r_j^s - r_k^s}{r_i^s - r_k^s}, & i \neq j, \\ \frac{1}{2} ([\pi_i^s(r_{N_p}^s)]^2 - [\pi_i^s(r_1^s)]^2), & i = j. \end{cases} \quad (\text{B10})$$

The surface term arising from the integration by parts in the derivation of Eq. (B9) is omitted, which amounts to the R -matrix boundary condition for the solution of Eq. (1) at $r = r_m$. The matrices $\mathcal{C}_{lm, l'm'}$ and $\mathcal{S}_{lm, l'm'}$ in Eq. (B8) are given by angular integrals and can be expressed in terms of the $3j$ symbols. For the present polarization (5) of the laser pulse we have

$$\begin{aligned} \mathcal{S}_{lm'l'm'} &= \langle Y_{lm} | \sin \theta \cos \varphi | Y_{l'm'} \rangle \\ &= (-1)^m \sqrt{\frac{(2l+1)(2l'+1)}{2}} \begin{pmatrix} l & 1 & l' \\ 0 & 0 & 0 \end{pmatrix} \left[\begin{pmatrix} l & 1 & l' \\ -m & -1 & m' \end{pmatrix} - \begin{pmatrix} l & 1 & l' \\ -m & 1 & m' \end{pmatrix} \right], \end{aligned} \quad (\text{B11a})$$

$$\begin{aligned} \mathcal{C}_{lm'l'm'} &= \langle Y_{lm} | \cos \theta | Y_{l'm'} \rangle \\ &= (-1)^m \sqrt{(2l+1)(2l'+1)} \begin{pmatrix} l & 1 & l' \\ 0 & 0 & 0 \end{pmatrix} \begin{pmatrix} l & 1 & l' \\ -m & 0 & m' \end{pmatrix}. \end{aligned} \quad (\text{B11b})$$

APPENDIX C: R-MATRIX METHOD FOR SCATTERING STATES

To facilitate the calculation of the projection in Eq. (7), the scattering states (17) must be calculated at the same radial quadrature points as used in the solution of Eq. (1). This can be achieved by using the R -matrix method [46] to solve Eq. (18). Let us consider the eigenvalue problem in the s th sector ($\bar{r}_{s-1} \leq r \leq \bar{r}_s$),

$$\left[-\frac{1}{2} \frac{d}{dr} r^2 \frac{d}{dr} + \frac{l(l+1)}{2} + r^2 V(r) + \mathcal{L}_s - r^2 \bar{E}_n \right] \bar{f}_{nl}(r) = 0, \quad (\text{C1})$$

where the Bloch operator [47]

$$\mathcal{L}_s = \frac{1}{2} r^2 [\delta(r - \bar{r}_s) - \delta(r - \bar{r}_{s-1})] \frac{d}{dr} \quad (\text{C2})$$

is introduced to Hermitize the Hamiltonian within the sector. The solutions are expanded in terms of the appropriate (Radau or Lobatto) DVR basis in the sector,

$$\bar{f}_{nl}(r) = \sum_{j=1}^{N_p} c_{jn}^{(l)s} \pi_j^s(r), \quad n = 1, \dots, N_p. \quad (\text{C3})$$

The expansion coefficients are obtained by solving the algebraic eigenvalue problem

$$\sum_{j=1}^{N_p} \bar{K}_{ij} c_{jn}^{(l)s} + \left[\frac{l(l+1)}{2} + r_i^2 V(r_i) - r_i^2 \bar{E}_n \right] c_{in}^{(l)s} = 0, \quad (\text{C4})$$

where the Hermitized kinetic energy operator (including the Bloch operator) is given by

$$\bar{K}_{ij} = \frac{1}{2} \sum_{k=1}^{N_p} \omega_k^s \frac{d\pi_i^s(r)}{dr} r^2 \frac{d\pi_j^s(r)}{dr} \Big|_{r=r_k^s}. \quad (\text{C5})$$

The solutions of Eq. (18) can be obtained in the form of a spectral expansion in terms of the eigensolutions of Eq. (C1),

$$\begin{aligned} f_{kl}(r) &= \frac{1}{r^2} \sum_{n=1}^{N_p} \frac{\bar{f}_{nl}(r)}{\bar{E}_n - E} \int_{\bar{r}_{s-1}}^{\bar{r}_s} \bar{f}_{nl}(r) \mathcal{L}_s f_{kl}(r) dr \\ &= \frac{1}{2r^2} \sum_{n=1}^{N_p} \frac{\bar{f}_{nl}(r)}{\bar{E}_n - E} \left[\bar{f}_{nl}(\bar{r}_s) d_{kl}(\bar{r}_s) \bar{r}_s^2 \right. \\ &\quad \left. - \bar{f}_{nl}(\bar{r}_{s-1}) d_{kl}(\bar{r}_{s-1}) \bar{r}_{s-1}^2 \right], \end{aligned} \quad (\text{C6})$$

where $E = k^2/2$ and $d_{kl}(r) = df_{kl}(r)/dr$. The R matrix (which is a number for the present one-channel problem) is defined by

$$f_{kl}(r) = \mathcal{R}_{kl}(r) d_{kl}(r). \quad (\text{C7})$$

Its propagation from \bar{r}_{s-1} to \bar{r}_s through the s th sector is carried out by means of the relation [48]

$$\mathcal{R}_{kl}(\bar{r}_s) = R_{s,s} - R_{s,s-1} [R_{s-1,s-1} + \mathcal{R}_{kl}(\bar{r}_{s-1})]^{-1} R_{s-1,s}, \quad (\text{C8})$$

where

$$R_{s,s'} = \frac{1}{2} \sum_{n=1}^{N_p} \frac{\bar{f}_{nl}(\bar{r}_s) \bar{f}_{nl}(\bar{r}_{s'})}{\bar{E}_n - E}. \quad (\text{C9})$$

Starting with the initial condition $\mathcal{R}_{kl}(0) = 0$ and propagating the R matrix through N_s sectors, we obtain $\mathcal{R}_{kl}(r_m)$ at the matching radius. By matching the solution to the asymptotic form Eq. (19) we find the scattering phase shift,

$$\delta_l = \arctan \left[\frac{j_l(kr) - \mathcal{R}_{kl}(r) \frac{dj_l(kr)}{dr}}{y_l(kr) - \mathcal{R}_{kl}(r) \frac{dy_l(kr)}{dr}} \right]_{r=r_m}. \quad (\text{C10})$$

Once δ_l is obtained, the derivatives $d_{kl}(\bar{r}_s)$ at the sector boundaries are propagated backwards from $\bar{r}_{N_s} = r_m$ to $\bar{r}_0 = 0$ using the relations

$$d_{kl}(\bar{r}_{N_s}) = \left[\frac{dj_l(kr)}{dr} \cos \delta_l - \frac{dy_l(kr)}{dr} \sin \delta_l \right]_{r=r_m}, \quad (\text{C11a})$$

$$\begin{aligned} \bar{r}_{s-1}^2 d_{kl}(\bar{r}_{s-1}) &= [\mathcal{R}_{kl}(\bar{r}_{s-1}) + R_{s-1,s-1}]^{-1} \\ &\quad \times R_{s-1,s} \bar{r}_s^2 d_{kl}(\bar{r}_s). \end{aligned} \quad (\text{C11b})$$

Using this together with Eqs. (C3) and (C6), we obtain the normalized solutions of Eq. (18) at the FEDVR quadrature points,

$$\begin{aligned} f_{kl}(r_n) &= \frac{1}{2\sqrt{\omega_i^s} r_i^{s2}} \sum_{n=1}^{N_p} \frac{c_{in}^{(l)s}}{\bar{E}_n - E} \\ &\quad \times \left[\frac{c_{N_p n}^{(l)s}}{\sqrt{\omega_{N_p}^s}} \bar{r}_s^2 d_{kl}(\bar{r}_s) - \frac{c_{1n}^{(l)s}}{\sqrt{\omega_1^s}} \bar{r}_{s-1}^2 d_{kl}(\bar{r}_{s-1}) \right], \end{aligned} \quad (\text{C12})$$

where the subscript n on the left-hand side is given in terms of the i and s appearing on the right-hand side by Eq. (B3).

- [1] H. Niikura, F. Légaré, R. Hasbani, A. D. Bandrauk, M. Yu. Ivanov, D. M. Villeneuve, and P. B. Corkum, Sub-laser-cycle electron pulses for probing molecular dynamics, *Nature (London)* **417**, 917 (2002).
- [2] D. Pavičić, K. F. Lee, D. M. Rayner, P. B. Corkum, and D. M. Villeneuve, Direct Measurement of the Angular Dependence of Ionization for N_2 , O_2 , and CO_2 in Intense Laser Fields, *Phys. Rev. Lett.* **98**, 243001 (2007).
- [3] J. Wu, L. Ph. H. Schmidt, M. Kunitski, M. Meckel, S. Voss, H. Sann, H. Kim, T. Jahnke, A. Czasch, and R. Dörner, Multiorbital

Tunneling Ionization of the CO Molecule, *Phys. Rev. Lett.* **108**, 183001 (2012).

- [4] L. Holmgaard, J. L. Hansen, L. Kalthø j, S. L. Kragh, H. Stapelfeldt, F. Filsinger, J. Küpper, G. Meijer, D. Dimitrovski, M. Abu-samha, C. P. J. Martiny, and Lars Bojer Madsen, Photoelectron angular distributions from strong-field ionization of oriented molecules, *Nat. Phys.* **6**, 428 (2010).
- [5] I. Petersen, J. Henkel, and M. Lein, Signatures of Molecular Orbital Structure in Lateral Electron Momentum Distributions

- from Strong-Field Ionization, *Phys. Rev. Lett.* **114**, 103004 (2015).
- [6] C. Smeenk, L. Arissian, A. Staudte, D. M. Villeneuve, and P. B. Corkum, Momentum space tomographic imaging of photoelectrons, *J. Phys. B* **42**, 185402 (2009).
- [7] P. Eckle, M. Smolarski, P. Schlup, J. Biegert, A. Staudte, M. Schöffler, H. G. Muller, R. Dörner, and U. Keller, Attosecond angular streaking, *Nat. Phys.* **4**, 565 (2008).
- [8] P. Eckle, A. N. Pfeiffer, C. Cirelli, A. Staudte, R. Dörner, H. G. Muller, M. Büttiker, and U. Keller, Attosecond ionization and tunneling delay time measurements in Helium, *Science* **322**, 1525 (2008).
- [9] C. P. J. Martiny, M. Abu-samha, and L. B. Madsen, Counterintuitive angular shifts in the photoelectron momentum distribution for atoms in strong few-cycle circularly polarized laser pulses, *J. Phys. B* **42**, 161001 (2009).
- [10] A. N. Pfeiffer, C. Cirelli, M. Smolarski, D. Dimitrovski, M. Abu-samha, L. B. Madsen, and U. Keller, Attoclock reveals natural coordinates of the laser-induced tunnelling current flow in atoms, *Nat. Phys.* **8**, 76 (2012).
- [11] J. Maurer, D. Dimitrovski, L. Christensen, L. B. Madsen, and H. Stapelfeldt, Molecular-Frame 3D Photoelectron Momentum Distributions by Tomographic Reconstruction, *Phys. Rev. Lett.* **109**, 123001 (2012).
- [12] L. Torlina, F. Morales, J. Kaushal, I. Ivanov, A. Kheifets, A. Zielinski, A. Scrinzi, H. G. Muller, S. Sukiasyan, M. Ivanov, and O. Smirnova, Interpreting attoclock measurements of tunnelling times, *Nat. Phys.* **11**, 503 (2015).
- [13] T. J. Park and J. C. Light, Unitary quantum time evolution by iterative Lanczos reduction, *J. Chem. Phys.* **85**, 5870 (1986).
- [14] A. I. Kuleff, J. Breidbach, and L. S. Cederbaum, Multielectron wave-packet propagation: General theory and application, *J. Chem. Phys.* **123**, 044111 (2005).
- [15] T. N. Rescigno and C. W. McCurdy, Numerical grid methods for quantum-mechanical scattering problems, *Phys. Rev. A* **62**, 032706 (2000).
- [16] B. I. Schneider and N. Nygaard, Discrete variable representation for singular Hamiltonians, *Phys. Rev. E* **70**, 056706 (2004).
- [17] B. I. Schneider, L. A. Collins, and S. X. Hu, Parallel solver for the time-dependent linear and nonlinear Schrödinger equation, *Phys. Rev. E* **73**, 036708 (2006).
- [18] J. Henkel, M. Lein, V. Engel, and I. Dreisigacker, Adiabaticity in the lateral electron-momentum distribution after strong-field ionization, *Phys. Rev. A* **85**, 021402(R) (2012).
- [19] I. A. Ivanov, Evolution of the transverse photoelectron-momentum distribution for atomic ionization driven by a laser pulse with varying ellipticity, *Phys. Rev. A* **90**, 013418 (2014).
- [20] J.-W. Geng, L. Qin, M. Li, W.-H. Xiong, Y. Liu, Q. Gong, and L.-Y. Peng, Nonadiabatic tunneling ionization of atoms in elliptically polarized laser fields, *J. Phys. B* **47**, 204027 (2014).
- [21] O. I. Tolstikhin and T. Morishita, Adiabatic theory of ionization by intense laser pulses: Finite-range potentials, *Phys. Rev. A* **86**, 043417 (2012).
- [22] L. D. Landau and E. M. Lifshitz, *Quantum Mechanics (Non-relativistic Theory)* (Pergamon, Oxford, 1977).
- [23] R. G. Newton, *Scattering Theory of Waves and Particles* (Springer-Verlag, New York, 1982).
- [24] *Handbook of Mathematical Functions*, edited by M. Abramowitz and I. A. Stegun (Dover, New York, 1972).
- [25] L. V. Keldysh, Ionization in the field of a strong electromagnetic wave, *Zh. Eksp. Teor. Fiz.* **47**, 1945 (1964) [*Sov. Phys. JETP* **20**, 1307 (1965)].
- [26] A. M. Perelomov, V. S. Popov, and M. V. Terent'ev, Ionization of atoms in an alternating electric field, *Zh. Eksp. Teor. Fiz.* **50**, 1393 (1966) [*Sov. Phys. JETP* **23**, 924 (1966)] .
- [27] A. M. Perelomov, V. S. Popov, and M. V. Terent'ev, Ionization of atoms in an alternating electric field: II, *Zh. Eksp. Teor. Fiz.* **51**, 309 (1966) [*Sov. Phys. JETP* **24**, 207 (1967)].
- [28] F. H. M. Faisal, Multiple absorption of laser photons by atoms, *J. Phys. B* **6**, L89 (1973).
- [29] H. R. Reiss, Effect of an intense electromagnetic field on a weakly bound system, *Phys. Rev. A* **22**, 1786 (1980).
- [30] M. Lewenstein, K. C. Kulander, K. J. Schafer, and P. H. Bucksbaum, Rings in above-threshold ionization: A quasiclassical analysis, *Phys. Rev. A* **51**, 1495 (1995).
- [31] G. L. Yudin and M. Yu. Ivanov, Nonadiabatic tunnel ionization: Looking inside a laser cycle, *Phys. Rev. A* **64**, 013409 (2001).
- [32] O. I. Tolstikhin, T. Morishita, and S. Watanabe, Adiabatic theory of ionization of atoms by intense laser pulses: One-dimensional zero-range-potential model, *Phys. Rev. A* **81**, 033415 (2010).
- [33] P. A. Batishchev, O. I. Tolstikhin, and T. Morishita, Atomic Siegert states in an electric field: Transverse momentum distribution of the ionized electrons, *Phys. Rev. A* **82**, 023416 (2010).
- [34] L. Hamonou, T. Morishita, and O. I. Tolstikhin, Molecular Siegert states in an electric field, *Phys. Rev. A* **86**, 013412 (2012).
- [35] V. N. T. Pham, O. I. Tolstikhin, and T. Morishita, Molecular Siegert states in an electric field. II. Transverse momentum distribution of the ionized electrons, *Phys. Rev. A* **89**, 033426 (2014).
- [36] J. S. Briggs, V. I. Savichev, and E. A. Solov'ev, Hidden crossings and excitation of hydrogen by a slow electric pulse, *J. Phys. B* **33**, 3363 (2000).
- [37] O. I. Tolstikhin, T. Morishita, and L. B. Madsen, Theory of tunneling ionization of molecules: Weak-field asymptotics including dipole effects, *Phys. Rev. A* **84**, 053423 (2011).
- [38] B. M. Smirnov and M. I. Chibisov, The breaking up of atomic particles by an electric field and by electron collisions, *Zh. Eksp. Teor. Fiz.* **49**, 841 (1965) [*Sov. Phys. JETP* **22**, 585 (1966)].
- [39] T. Popmintchev, M.-C. Chen, D. Popmintchev, P. Arpin, S. Brown, S. Ališauskas, G. Andriukaitis, T. Balčiūnas, O. D. Mücke, A. Pugzlys, A. Baltuška, B. Shim, S. E. Schrauth, A. Gaeta, C. Hernández-García, L. Plaja, A. Becker, A. Jaron-Becker, M. M. Murnane, and H. C. Kapteyn, Bright coherent ultrahigh harmonics in the keV X-ray regime from mid-infrared femtosecond lasers, *Science* **336**, 1287 (2012).
- [40] G. L. Carr, M. C. Martin, W. R. McKinney, K. Jordan, G. R. Neil, and G. P. Williams, High-power terahertz radiation from relativistic electrons, *Nature (London)* **420**, 153 (2002).
- [41] V. I. Krylov, *Approximate Calculation of Integrals* (Dover, New York, 2005).
- [42] J. N. Reddy, *An Introduction to the Finite Element Method* (McGraw-Hill, New York, 2005).
- [43] D. O. Harris, G. G. Engerholm, and W. D. Gwinn, Calculation of matrix elements for one-dimensional quantum-mechanical

- problems and the application to anharmonic oscillators, *J. Chem. Phys.* **43**, 1515 (1965).
- [44] A. S. Dickinson and P. R. Certain, Calculation of matrix elements for one-dimensional quantum-mechanical problems, *J. Chem. Phys.* **49**, 4209 (1968).
- [45] J. C. Light, I. P. Hamilton, and J. V. Lill, Generalized discrete variable approximation in quantum mechanics, *J. Chem. Phys.* **82**, 1400 (1985).
- [46] P. G. Burke, *R-Matrix Theory of Atomic Collisions: Application to Atomic, Molecular and Optical Processes* (Springer, Berlin, 2011).
- [47] C. Bloch, Une formulation unifiée de la théorie des réactions nucléaires, *Nucl. Phys.* **4**, 503 (1957).
- [48] K. L. Baluja, P. G. Burke, and L. A. Morgan, *R*-matrix propagation program for solving coupled second-order differential equations, *Comput. Phys. Commun.* **27**, 299 (1982).